Climate Dynamics (2019) 53:5529–5546
https://doi.org/10.1007/s00382-019-04879-x

A coupled moisture-dynamics model of the Madden–Julian oscillation: convection interaction with first and second baroclinic modes and planetary boundary layer

Tim Li[1,2] **· Feng Hu**[1]

Received: 7 January 2019 / Accepted: 24 June 2019 / Published online: 16 July 2019

Abstract
A theoretical model with a single prognostic variable, column-integrated moist static energy (MSE), was constructed to understand the dynamics of MJO eastward propagation and planetary scale selection. A key process in the model is the interaction of MSE-dependent convection with free-atmospheric first, second baroclinic modes and planetary boundary layer. Under a realistic parameter regime, the model reproduces the most unstable mode at zonal wavenumber 1 with a slow eastward phase speed of about 5 ms^{-1}. The slow eastward phase speed in the model arises from the competition of eastward moving MSE tendencies caused by horizontal MSE advection, vertical MSE advection and boundary layer moistening with westward moving tendencies contributed by surface latent heat flux and atmospheric longwave radiative heating. The planetary scale selection is primarily attributed to the phase lag of longwave radiative heating associated with upper-level stratiform clouds that occur in the rear of MJO deep convection.

Keywords MJO theoretical model · A coupled moisture-dynamics mode · Eastward propagation · Planetary scale selection · Stratiform cloud

1 Introduction

The Madden–Julian oscillation (MJO; Madden and Julian 1971, 1972) is a dominant intraseasonal mode in the tropics (see Li and Hsu 2018 for a book review on this topic). It is characterized by slow eastward propagation of around 5 ms^{-1} along the equator over the Eastern Hemisphere (Knutson 1986; Lau and Chan 1986; Hendon and Salby 1994; Lau and Lau 2010) and zonal planetary scale (Zhang 2005; Li and Zhou 2009; Li 2014). In the energy power spectrum, the MJO mode is well distinguished from convectively coupled equatorial waves (Wheeler and Kiladis 1999; Kiladis et al. 2009).

Early theoretical studies regarded the MJO as a moist Kelvin wave interacting with convective heating through the wave-CISK (conditional instability of the second kind) mechanism (Chang and Lim 1988), but so derived MJO mode had a too fast phase speed and was favorable for growth of shorter waves (Wang and Chen 1989). Emanuel (1987) proposed a wind-induced surface heat exchange (WISHE) theory but this theory depends on the presence of the mean easterly in the tropics. In reality the MJO is most active over the Indo-Pacific warm pool where the mean westerly is pronounced (Wang 1988a). Wang and Li (1994) and Li and Wang (1994) proposed a convection—frictional convergence (CFC) feedback theory in which free-atmospheric first-baroclinic mode Rossby and Kelvin waves are coupled with planetary boundary layer (PBL) by convective heating. Various observational characteristics of the MJO, such as slow and longitude-dependent eastward phase speed, horizontal pattern of Kelvin–Rossby wave couplet, and a phase leading of PBL convergence to the main convection center (Hendon and Salby 1994; Jones and Weare 1996; Maloney and Hartmann 1998; Chao and Chen 1999; Moskowitz and

✉ Feng Hu
690953768@qq.com

[1] Key Laboratory of Meteorological Disaster, Ministry of Education/Joint International Research Laboratory of Climate and Environmental Change/Collaborative Innovation Center on Forecast and Evaluation of Meteorological Disasters, Nanjing University of Information Science and Technology, Nanjing, China

[2] Department of Atmospheric Sciences, School of Ocean and Earth Science and Technology, University of Hawaii at Manoa, Honolulu, HI, USA

Bretherton 2000; Sperber 2003), were reproduced by the model. However, under a linear heating, the MJO mode in the model prefers the growth of shorter wavelength, and only under a nonlinear heating did the model generate the most unstable mode at wavenumber 1 (Li and Zhou 2009).

Recently there has been a growing body of theoretical work for the MJO. Building upon previous versions of the skeleton model (Majda and Biello 2004, Biello et al. 2007; Khouider and Majda 2006, 2007; Majda and Stechmann 2009), Thual et al. (2015) constructed a stochastic skeleton model. The essential physical process in the model is scale interaction among planetary dry dynamics, planetary lower tropospheric moisture, and the planetary envelope of synoptic-scale eddies. Under a controlled set of parameters, the model reproduces a neutrally stable atmospheric wave solution, with the intermittent generation of MJO events. Various assumptions have been made to close the system. The most important one is the dependence of tendency of planetary envelope of synoptic-scale eddies on planetary-scale lower tropospheric moisture. Such an assumption requires further observational validation.

Sobel and Maloney (2012, 2013) constructed a simple theoretical model with the use of column-integrated specific humidity as a single prognostic variable. The circulation anomaly was determined empirically. Thus strictly speaking, this model is a semi-empirical model as the dynamics governing equations are not derived from the first principal. The essence of the model is the "moisture mode" paradigm in which processes that control column integrated humidity tendency hold a key for the eastward propagation (Maloney 2009; Hsu and Li 2012). Unfortunately, the original model of Sobel and Maloney (2012) reproduced a preferred westward phase speed, which is at odds with the observation. Adames and Kim (2016) extended the original Sobel–Maloney model framework by adding the first baroclinic mode shallow water model equations and assuming that precipitation anomaly is proportional to column integrated specific humidity anomaly. The main process for eastward propagation in the model lies in the advection of mean moisture by anomalous meridional wind, which differs from the original Sobel–Maloney model in which the anomalous zonal advection by the background mean flow is the sole factor for eastward propagation.

Motivated by the moisture mode paradigm, Wang and Chen (2017) extended the original 2.5-layer model of Wang and Li (1994) and Li and Wang (1994) by incorporating the moisture feedback to precipitation with a simplified Betts-Miller cumulus parameterization scheme (Liu and Wang 2017). The model reproduces a more realistic MJO with slower eastward phase speed. Wang and Chen (2017) argued that slowing down of eastward propagation compared to the original model of Wang and Li (1994) with Kuo (1974) cumulus parameterization scheme is attributed to strengthened coupling between precipitation and Rossby waves in the Betts-Miller scheme. However, this Rossby wave dragging hypothesis was recently challenged by Wang et al. (2018), who demonstrated based on both Aqua planet simulations and the diagnosis of 27 MJOTF/GASS models (Jiang et al. 2015) that a stronger Rossby wave component favors faster eastward propagation due to enhanced east–west asymmetry of MSE tendency.

So far, there is no satisfactory explanation of MJO planetary scale selection by a linear model. Early attempt with a 2.5-layer model by Wang (1988b) showed a preferred planetary zonal wavelength when a longwave approximation is assumed. Using a 2.5-layer model with the CFC feedback, Li and Zhou (2009) demonstrated that the model generates the most unstable mode at a short wavelength under a linear heating, and a long wave selection can only be achieved when a nonlinear conditional heating is specified. Physical interpretation behind this nonlinear wave interference mechanism is that dry Kelvin waves move much faster than wet (convectively coupled) Kelvin waves so that higher wavenumber perturbations are gradually damped. This nonlinear wave interference mechanism was further confirmed by Wei et al. (2017) using a simple analytical model that contains both the moisture mode and the CFC feedback paradigm.

Whereas a few modeling works stressed the importance of stratiform clouds in MJO simulation (e.g., Fu and Wang 2009; Zhang and Song 2009), most of previous theoretical models of the MJO neglected atmospheric second baroclinic mode motion. In a recent model diagnostic study, Wang et al. (2017) demonstrated that the main difference between a "good" model group (containing seven best MJO propagation models) and a "poor" model group (containing seven worst models) lies in their capability in capturing the observed east–west asymmetry of vertical MSE advection. While the main deep convective heating center is characterized by first baroclinic mode vertical velocity profile, there is marked zonal asymmetry in anomalous vertical velocity field to the east and west of the main convection. The anomalous vertical velocity field in these regions is characterized mainly by the second baroclinic mode vertical profile (Wang et al. 2017). To the east of the main MJO convection, subsidence is pronounced in the upper troposphere while ascending motion anomaly appears in the lower troposphere. An opposite vertical velocity anomaly field is observed to the west of the main MJO convective center. Given the mean MSE profile (with maxima in tropopause and near the surface and a minimum in middle troposphere), such a vertical velocity pattern induces a positive (negative) MSE tendency to the east (west) of the MJO convection, favoring eastward propagation. The vertically tilting vertical velocity structure is consistent with the observed feature of upper-level stratiform cloud deck in the rear and lower-level congestus clouds in the front.

Motivated by the aforementioned observational, theoretical and modeling studies, we intend to build a unified theoretical framework that contains the essence of the CFC and the moisture mode paradigms, with explicit description of time change rate of column integrated MSE and governing equations for free-atmospheric first and second baroclinic mode motions. The goal of this theoretical model is to seek an analytical solution to understand the relative roles of various processes in contributing to MJO slow eastward phase propagation and planetary sale selection. By constructing a linear model that contains all existing physical processes that affect the MSE tendency, one may analyze the relative role of different processes in contributing to the slow eastward phase speed and planetary scale selection. The remaining part of this paper is organized as followings. In Sect. 2, a theoretical model framework is constructed step-by-step. In Sect. 3, we show the model dispersion relation and theoretical solutions. The physical mechanisms for the slow eastward propagation and planetary scale selection are discussed in Sects. 4 and 5, respectively. Finally, a conclusion and discussion are given in the last section.

2 Model formulation

Figure 1a shows the lagged time—longitude diagrams of regressed rainfall and MSE anomalies based on observational data. The column-integrated MSE anomaly follows the rainfall anomaly closely, which suggests that to the first order of approximation, the MSE anomaly may be regarded as a key variable to represent the MJO convective envelope. At day 0 when MJO convection and MSE center are located at 80 °E, there is a clear zonal asymmetry in the MSE tendency field, with a positive tendency to the east and a negative tendency to the west of the MSE center (Fig. 1b). The essence of the moisture mode paradigm is that it is the zonal asymmetry of the MSE tendency that causes the eastward propagation of the MJO. Thus, understanding the cause of the zonal asymmetry of MSE tendency becomes critical for understanding the MJO propagating behavior.

Given that the MSE is a conservative quantity in the tropics (Neelin and Held 1987) and that MJO convective rain band is in general in phase with the anomalous MSE center (e.g., Jiang et al. 2015; Wang et al. 2017), it is desirable to construct a simple theoretical framework with anomalous MSE as a key variable. The column-integrated MJO-scale MSE budget equation may be written as following:

$$\left\langle \partial_t m' \right\rangle = \left\langle -\vec{V} \bullet \nabla m \right\rangle' - \left\langle \omega \partial_p m \right\rangle' + \left\langle \dot{Q}'_R \right\rangle + Q'_{LH} \qquad (1)$$

where $m' = c_p T' + gz' + L_v q'$ represents MSE anomaly, T' is anomalous temperature, z' is height anomaly, q' is specific humidity anomaly, c_p is the specific heat at constant pressure (1004 JK^{-1} kg^{-1}), g is the gravitational acceleration (9.8 ms^{-2}), L_v is the latent heat of vaporization (2.5×10^6 $J\,kg^{-1}$), $\vec{V}$ is horizontal wind vector, and ω is vertical pressure velocity. A prima represents MJO-scale component, and an angle bracket denotes a mass-weighted vertical integral from top of tropopause at P_T (100 hPa) to the surface at P_s (1000 hPa): $\langle A \rangle = \int_{P_T}^{P_s} \frac{1}{g} A dp$, where A represents a given variable and p is pressure. The first and second terms on right hand side of Eq. (1) represent horizontal and vertical MSE advection, respectively, the third term ($\langle \dot{Q}'_R \rangle$) represents the sum of vertically integrated anomalous shortwave and longwave radiative heating rate, the fourth term (Q'_{LH}) denotes the surface latent heat flux anomaly. In the equation above, we neglect anomalous surface sensible heat flux as it is small.

An observational diagnosis of anomalous MSE budget by Wang et al. (2017) showed that the horizontal and

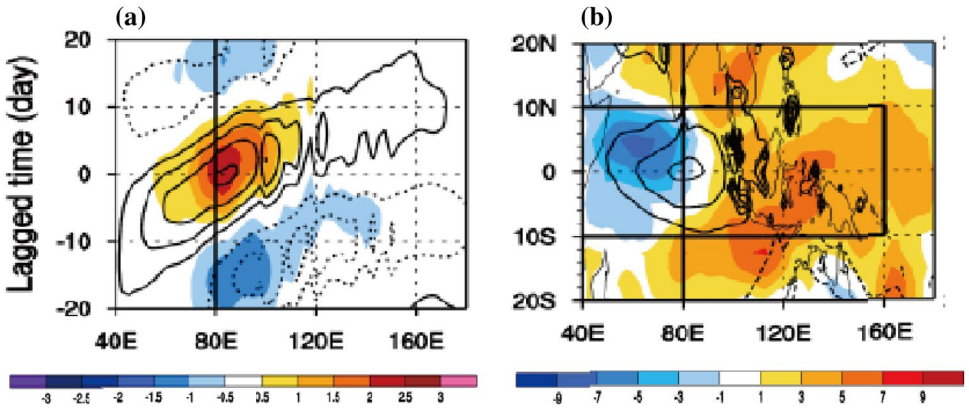

Fig. 1 **a** Longitude-time section of rainfall anomalies (shaded, units: mm day^{-1}) and column-integrated MSE anomalies (contour; units: J m^{-2}) averaged over 10°S–10°N regressed against 20–100 day band-pass-filtered rainfall anomaly over the equatorial eastern Indian Ocean (75°–85°E, 5°S–5°N). **b** Regressed column-integrated MSE tendency anomaly (shaded, units: W m^{-2}) and MSE anomaly (contour; units: J m^{-2}) at day 0. From Wang et al. (2017)

vertical MSE advection terms in the free atmosphere are primarily determined by the advection of mean MSE by anomalous meridional and vertical velocity. Compared to the meridional advection, anomalous zonal advection is small. Therefore the sum of column integrated horizontal and vertical advection terms may be approximated as

$$\left\langle -\vec{V}\bullet\nabla m\right\rangle' - \left\langle \omega\partial_p m\right\rangle' \doteq \frac{1}{g}\int_{P_T}^{P_B}\left(-v'\partial_y\bar{m}\right)dp - \frac{1}{g}\int_{P_T}^{P_B}\left(\omega'\partial_p\bar{m}\right)dp + \delta\partial_t m'_B \tag{2}$$

where P_B denotes the pressure at top of PBL, $\partial_t m'_B$ denotes the mean MSE tendency at PBL, $\delta = \frac{\Delta P_B}{g}$, and $\Delta P_B = P_S - P_B$. A bar denotes the background mean state. We further assume that the MSE tendency at PBL is primarily determined by that of the moisture component. Thus, the column integrated anomalous MSE equation may be approximated as

$$\left\langle \partial_t m'\right\rangle \doteq \frac{1}{g}\int_{P_T}^{P_B}\left(-v'\partial_y\bar{m}\right)dp - \frac{1}{g}\int_{P_T}^{P_B}\left(\omega'\partial_p\bar{m}\right)dp + \left\langle \dot{Q}'_R\right\rangle + Q'_{LH} + \delta L_v\partial_t q'_B \tag{3}$$

Physical processes associated with the first two terms in the right hand side of Eq. (3) may be expressed as following. To the east of the MJO convection, anomalous poleward flows induced by suppressed convection east of MJO convection tend to generate a positive MSE tendency through the anomalous advection of the mean MSE (Kim et al. 2014). To its west, anomalous low-level Rossby wave cyclonic gyres tend to generate a negative MSE tendency through anomalous meridional advection of the mean MSE. According to the observation, the horizontal wind anomaly in the free atmosphere shows a prominent first baroclinic mode structure (Wang et al. 2017).

Different from the horizontal motion, MJO-scale vertical velocity field exhibits a distinctive second baroclinic mode structure away from the deep convective center (Mapes 2000; Wang et al. 2017). To the east of MJO convective center, a pronounced descending anomaly appears in the upper troposphere and an ascending anomaly appears in lower troposphere. To the west, an opposite profile is observed, with a pronounced ascending anomaly appearing in the upper tropospheric stratiform cloud region and a descending anomaly in the lower troposphere. Assuming that the mean MSE vertical profile has a minimum in the middle troposphere (Fig. 2), such a second baroclinic mode vertical velocity anomaly would lead to a positive (negative) MSE tendency to the east (west). The MSE advection by the first baroclinic mode vertical velocity, on the other hand, would be negligibly small and thus is not considered in the current model framework.

The discussion above emphasizes the important contributions of both the free-atmospheric first and second baroclinic mode motion. Thus, we will first derive governing equations for the first and second baroclinic mode. Figure 2 shows the vertical profiles of horizontal velocity, geopotential height and vertical velocity fields for the first and second baroclinic modes. For the first (second) baroclinic mode, horizontal velocity and geopotential height fields are written at 700 hPa (500 hPa) and vertical velocity and diabatic heating fields are written at 500 hPa (300 hPa).

The first baroclinic mode governing equations may be written as:

$$\begin{cases} \varepsilon u'_1 - \beta y v'_1 = -\partial_x\phi'_1 \\ \beta y u'_1 = -\partial_y\phi'_1 \\ \varepsilon\phi'_1 + C_1^2\left(\partial_x u'_1 + \partial_y v'_1\right) = -\frac{\dot{Q}'_1}{C_p}\frac{R\Delta P_1}{2P_1} \end{cases} \tag{4}$$

where ε is the damping coefficient at free atmosphere, ϕ is geopotential height, C_1 denotes gravity wave speed for the first baroclinic mode (50 $\mathrm{m\,s^{-1}}$), Q_1 represents atmospheric diabatic heating, R is gas constant for dry air (287 $\mathrm{J\,K^{-1}\,kg^{-1}}$), $P_1 = 500$ hPa denotes pressure level in middle troposphere, and $\Delta P_1 = 800$ hPa represents the depth of free atmosphere.

In a simplified Betts-Miller scheme the precipitation anomaly is proportional to column integrated specific humidity (Wang and Chen 2017). On the other hand, as shown in Fig. 1, MJO-scale precipitation and column integrated MSE fields have similar horizontal structure and propagation characteristics. Thus one may directly link $\langle m'\rangle$ to the diabatic heating anomaly at the equator, that is,

$$\frac{\dot{Q}'_1}{C_p}\frac{R\Delta P_1}{2P_1}\Big|_{y=0} = b_1\left\langle m'\right\rangle\Big|_{y=0}, \tag{5}$$

where coefficient b_1 can be determined empirically based on the observed scattering relationship (Fig. 3a). Correlation coefficient between a linear fitting function and observed data is 0.77, which passes a 99% confidence level with a student-t test.

Through a series of derivation (see Appendix for detailed derivation), the meridional wind anomaly of the first baroclinic mode may be written as:

$$v'_1 = -b_1 y M e^{-\frac{y^2}{2}\frac{\beta}{C_1}} e^{i(kx-\sigma t)} D_1. \tag{6}$$

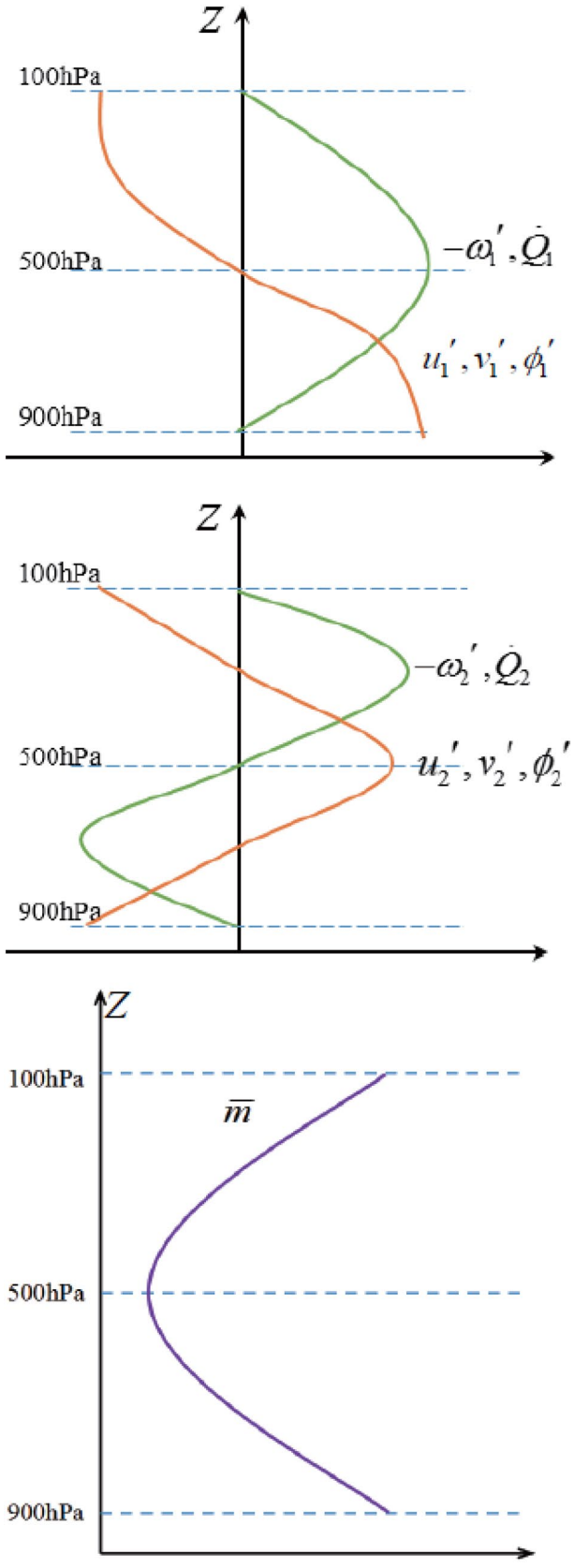

Fig. 2 Vertical profiles of key variables for (top) the first baroclinic mode, (center) the second baroclinic mode and (bottom) vertical profile of an idealized background mean MSE field. Green (orange) lines represent the profiles of vertical velocity and diabatic heating (horizontal velocity and geopotential height). Variables are defined at specific pressure levels. Subscript 1 and 2 represent variables for first and second baroclinic mode respectively. Purple line represent mean profile of MSE

The second baroclinic mode governing equations may be written as:

$$\begin{cases} \varepsilon u_2' - \beta y v_2' = -\partial_x \phi_2' \\ \beta y u_2' = -\partial_y \phi_2' \\ \varepsilon \phi_2' + C_2^2 \left(\partial_x u_2' + \partial_y v_2'\right) = -\frac{\dot{Q}_2'}{C_p} \frac{R\Delta P_2}{2P_2} \end{cases} \tag{7}$$

where C_2 denotes gravity wave speed for the second baroclinic mode ($26.2\,\mathrm{ms}^{-1}$), $P_2 = 300\,\mathrm{hPa}$ denotes pressure level where maximum stratiform heating is located, $\Delta P_2 = 400\,\mathrm{hPa}$ represents the half depth of free atmosphere, and others are conventional variables. For the detailed derivation of the first and second baroclinic mode governing equations, readers are referred to Li and Hsu (2018) (Chapter 1).

The diabatic heating process associated with the second baroclinic mode away from the deep convective center is primarily controlled by stratiform heating in the rear and by low-level congestus heating in the front. Following the method applied to the first baroclinic mode, one may derive a linear relationship between the upper-tropospheric stratiform heating in the rear and the column integrated MSE anomaly at the equator. Mathematically, Q_2 may be parameterized as

$$\frac{\dot{Q}_2'}{C_p} \frac{R\Delta P_2}{2P_2}\Big|_{y=0} = b_2 \langle m' \rangle (t, x + x_1)\Big|_{y=0}. \tag{8}$$

Figure 3b illustrates the relationship between the diabatic heating in the rear upper troposphere and the column integrated MSE anomaly over the MJO convective center. The correlation coefficient between a linear fitting function and the observed data is 0.59, which passes a 99% confidence level with a student-t test. Note that a lagged correlation between the two quantities was also calculated, and the result shows that maximum correlation occurs at the simultaneous time. Thus no time lag is assumed between the two in Eq. (8).

Through a series of derivation, the vertical velocity anomaly of the second baroclinic mode may be written as:

$$\omega_2' = -\Delta P_2 b_2 M e^{-\frac{y^2}{2}\frac{\beta}{C_2}} e^{i(kx-\sigma t)} e^{i(kx_1)} D_2(y^2) \tag{9}$$

With the derivation of the first-baroclinic-mode meridional wind and the second-baroclinic-mode vertical velocity

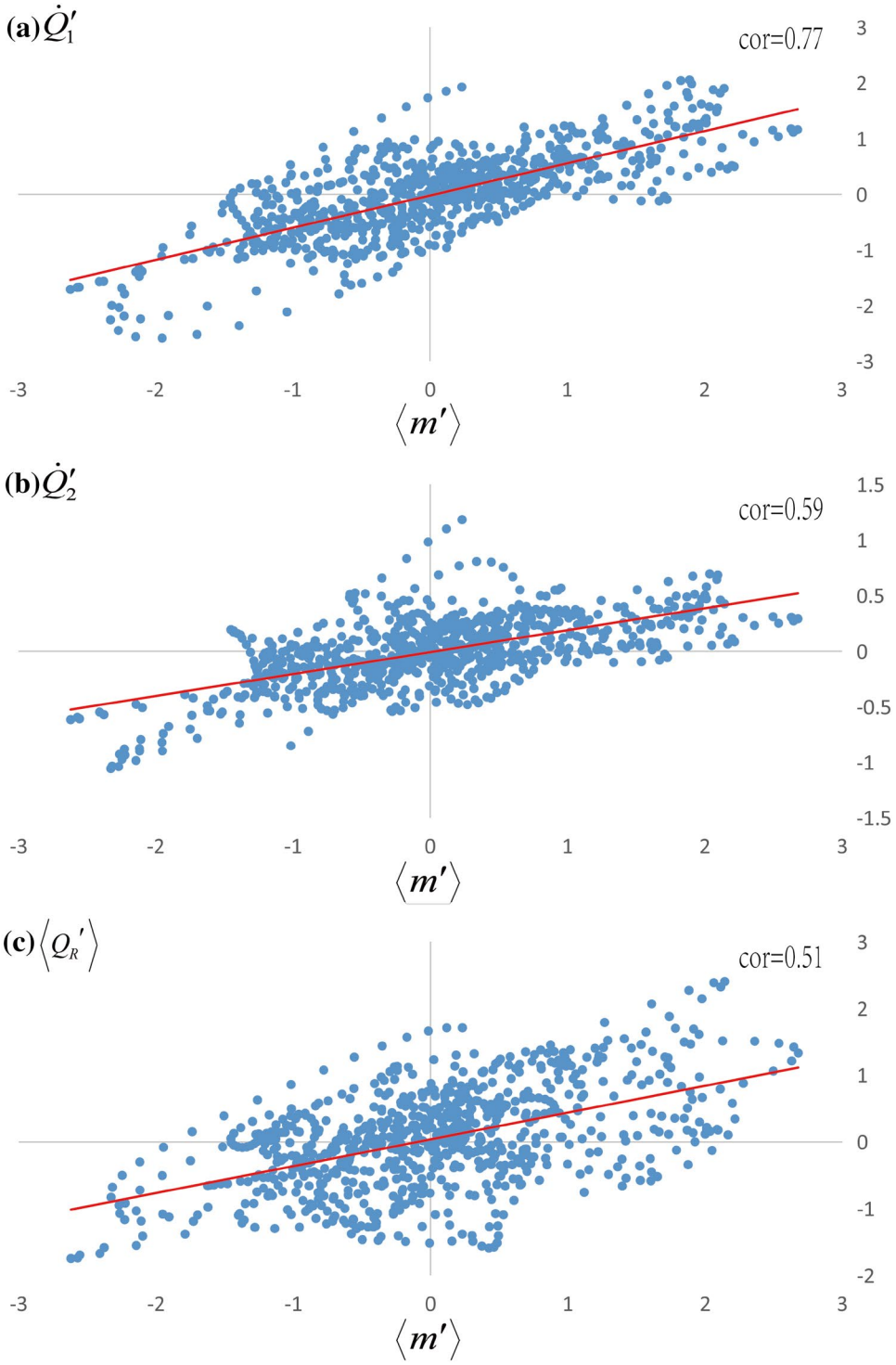

Fig. 3 Scattering diagrams for **a** column-integrated MSE (x-axis; units: 10^7 J m^{-2}) and mid-tropospheric diabatic heating (y-axis, unit: K day^{-1}) over MJO convective center (75°–85°E, 10°S–10°N), **b** column-integrated MSE at the MJO center and diabatic heating in upper troposphere (averaged over 500–200 hPa, y-axis) west of the MJO center (55°–75°E, 10°S–10°N; unit: K day^{-1}), and **c** column-integrated MSE and column integrated radiative heating rate (y-axis; unit: K day^{-1}) over the MJO center. Here diabatic heating fields were calculated based on European Centre for Medium-Range Weather Forecast (ECMWF) reanalysis date (ERA-Interim, Dee et al. 2011) with a horizontal resolution of 1.5° latitude by 1.5° longitude, and shortwave and longwave radiative heating fields were obtained from Modern-Era Retrospective Analysis for Research and Applications (MERRA) (Rienecker et al. 2011), for an analysis period of 1979–2008

anomaly fields, the first two terms in the right hand side of Eq. (3) are resolved. Next, we derive the radiative heating—MSE relationship. This term is primarily controlled by longwave radiative heating. It has been shown that this term generally contributes positively to the MSE tendency in cloud covered regions and plays an important role in maintaining the MJO strength (Jiang et al. 2015; Adames and Kim 2016). Due to the occurrence of the stratiform cloud in the rear, this term also contributes to the zonal asymmetry in the MSE tendency, favoring a westward phase speed (Wang et al. 2017).

A simple way to describe the longwave radiative effect in the current theoretical framework is to relate the column integrated radiative heating anomaly to the MSE anomaly. A linear fitting function $\langle \dot{Q}_R' \rangle = \alpha_1 \langle m' \rangle + \alpha_2 \langle m' \rangle (t, x + x_1)$

is assumed and coefficients α_1 and α_2 are determined empirically based on the observational data over the deep convective and stratiform cloud regions respectively. Figure 3c shows the observed scattering diagram over the deep convective cloud region. The correlation coefficient between the fitting function and the observed data is 0.51, which passed a 99% confidence level with a student-t test. A similar significant relationship is found over the stratiform cloud region (figure not shown). The amplitude of the slope over the convective cloud region, however, is about four times as large as that over the stratiform cloud region.

To calculate the surface latent heat flux (term 4 in the right hand side of Eq. 3) and PBL MSE changes (term 5 in the right hand side of Eq. 3) contribution, a vertically integrated PBL model (Wang and Li 1993) is introduced:

$$\begin{cases} Eu'_B - \beta y v'_B = -\partial_x \phi'_B \\ Ev'_B + \beta y u'_B = -\partial_y \phi'_B \\ \partial_x u'_B + \partial_y v'_B + \frac{\omega'_B}{\Delta P_B} = 0 \\ \phi'_B = \phi'_1 - \phi'_2 \end{cases} \tag{10}$$

where E denotes Ekman damping coefficient, subscript B denotes the boundary layer variable, ϕ_B denotes geopotential height anomaly at top of PBL, which is the sum of geopotential height anomalies associated with the first and second baroclinic modes. Through a series of derivation, anomalous zonal wind at PBL, u'_B, and anomalous vertical velocity at top of PBL, ω'_B, may be written as:

$$u'_B = b_1 M e^{-\frac{y^2}{2}\frac{\beta}{C_1}} e^{i(kx-\sigma t)} D_3(y^2) - b_2 M e^{-\frac{y^2}{2}\frac{\beta}{C_2}} e^{i(kx-\sigma t)} e^{ikx_1} D_4(y^2) \tag{11}$$

$$\begin{aligned} \omega'_B = {} & \Delta P_B b_1 M e^{-\frac{y^2}{2}\frac{\beta}{C_1}} e^{i(kx-\sigma t)} D_5(y^2) \\ & + \Delta P_B b_2 M e^{-\frac{y^2}{2}\frac{\beta}{C_2}} e^{i(kx-\sigma t)} e^{ikx_1} D_6(y^2) \end{aligned} \tag{12}$$

The surface latent heat flux anomaly may be written as

$$Q'_{LH} = \left[C_E \rho_a L_v (q_s - q_a) \left| \vec{V}_B \right| \right]', \tag{13}$$

where C_E is exchange coefficient (1.5×10^{-3}), ρ_a denotes air density at the standard sea level (1.225 kg m^{-3}), q_s denotes specific humidity at sea surface, and q_a is specific humidity at 10 m.

For simplicity, we neglect the effect of sea-air specific humidity difference anomaly and assume that MJO-scale latent heat flux anomaly is primarily determined by anomaly zonal wind. The total surface wind speed may be linearly decomposed into the following two terms:

$$\begin{aligned} \left| \vec{V}_B \right| &= \sqrt{u_B^2 + v_B^2} = \sqrt{\left(\bar{u}_B + u'_B\right)^2 + \left(\bar{v}_B + v'_B\right)^2} \\ &= \sqrt{\left(\bar{u}_B^2 + \bar{v}_B^2\right)\left(1 + \frac{2\bar{u}_B u'_B}{\bar{u}_B^2 + \bar{v}_B^2}\right)} \\ &= \left|\bar{V}_B\right| \sqrt{1 + \frac{2\bar{u}_B u'_B}{\bar{u}_B^2 + \bar{v}_B^2}} \approx \left|\bar{V}_B\right| \left(1 + \frac{\bar{u}_B u'_B}{\bar{u}_B^2 + \bar{v}_B^2}\right) \\ &= \left|\bar{V}\right|_B + \frac{\bar{u}_B u'_B}{\left|\bar{V}_B\right|} \end{aligned} \tag{14}$$

Substituting (14) into Eq. (13), one may obtain

$$Q'_{LH} = C_E \rho_a L_v (\bar{q}_s - \bar{q}_a) \frac{\bar{u}_B u'_B}{\left|\bar{V}_B\right|}. \tag{15}$$

Therefore, for given the mean westerly over the warm pool, an easterly (westerly) anomaly to the east (west) of the MJO center would lead to reduced (strengthened) surface latent heat flux, which favors a westward MSE tendency and thus a westward phase speed. The result is consistent with the observational analysis (e.g., Jiang et al. 2015; Wang et al. 2017).

Observational analyses (e.g., Hsu and Li 2012) showed that a positive tendency of PBL specific humidity often appears in front of MJO convection, and this positive tendency is primarily attributed to the advection of mean moisture by anomalous ascending motion associated with PBL convergence. Thus, the PBL MSE tendency equation may be written as:

$$\delta L_v \partial_t q'_B = -\delta L_v \omega'_B \partial_p \bar{q}_B. \tag{16}$$

The derivations above lead to a single variable equation for the column- integrated MSE anomaly:

$$\begin{aligned} \left\langle \partial_t m' \right\rangle = {} & \frac{\Delta P_2}{g} \left(-v'_1 \partial_y \bar{m}\right)\Big|_{p=700\,\mathrm{hPa}} - \frac{\Delta P_1}{g} \left(\omega'_2 \partial_p \bar{m}\right)\Big|_{p=300\,\mathrm{hPa}} \\ & + \alpha \left\langle m' \right\rangle + \rho_a C_E L_v (\bar{q}_s - \bar{q}_a) \frac{\bar{u}_B u'_B}{\left|\bar{V}_B\right|} - L_v \frac{\Delta P_B}{g} \omega'_B \partial_p \bar{q}_B \end{aligned} \tag{17}$$

where $\partial_y \bar{m}$ represents the meridional gradient of observed northern winter mean MSE field at 700 hPa averaged over the Indo-Pacific warm pool region (80°E–160°E), $\partial_p \bar{m}$ and $\partial_p \bar{q}_B$ denote the vertical gradients of observed northern winter mean MSE field at 300 hPa and mean specific humidity at PBL averaged over the same longitudinal zone, and $\bar{u}_B$ denotes observed winter mean surface zonal wind averaged over the warm pool region. Because the horizontal gradient of mean MSE is small in upper troposphere, we only consider the lower-tropospheric meridional advection in

Eq. (17). For the vertical advection term (the second term in the right-hand side of Eq. 17), we consider both the lower and upper tropospheric advective processes.

The observed column integrated MSE anomaly field shows a Gausian meridional structure (Wang et al. 2017). Thus, to the first order of approximation, we assume the following solution for $\langle m' \rangle$: $\langle m' \rangle = M\, e^{-\frac{y^2}{2L_0^2}} e^{i(kx-\sigma t)}$, where $L_0 = \sqrt{\frac{C_0}{\beta}}$ represents meridional e-folding length scale. Substituting Eqs. (6, 9, 11 and 12) into Eq. (17) and integrating Eq. (17) meridionally from $-L_0$ to L_0, one may derive a dispersion equation. Let $\sigma = \sigma_R + i\sigma_I$, where σ_R denotes frequency and σ_I denotes growth rate. Then both the frequency and growth rate are function of zonal wavenumber k, and can be calculated based on the dispersion equations (see the Appendix for detailed derivation).

It is worth mentioning that a number of key assumptions have been made in the simple analytical framework. Firstly, we neglect the time change rate of the first and second baroclinic mode motions. Secondly an empirical relation between anomalous precipitation and MSE fields and a longitudinal phase difference between the stratiform and deep convective center are assumed. Thirdly, a lowest meridional mode structure for the MSE is assumed so that a simple analytical dispersion relation between frequency/growth rate and zonal wavenumber can be derived.

3 Analytical solutions

3.1 Frequency and growth rate

Given a zonal wavenumber k, frequency and growth rate of the simple analytical model can be determined. The zonal phase speed can be further derived by the following formula: $C = \sigma_R/k$.

The standard values of the model key parameters are listed in Table 1. Figure 4 shows so calculated frequency, growth rate and phase speed using standard parameter values listed in Table 1. In the presence of all five physical processes (right hand side of Eq. 2), the model generates a slow eastward phase speed, with the maximum growth rate at zonal wavenumber 1.

With the increase of zonal wavenumber or decrease of zonal wavelength, both the growth rate and the phase speed decrease. For wavenumber 1, the growth rate is 0.18 day^{-1}, corresponding to an e-folding scale of 10 days. This amplification rate is within the observed range for the MJO-scale motion (Wang and Li 1994). The corresponding phase speed is 5.2 m s^{-1}, which is similar to the observed MJO phase propagation speed over the warm pool.

To understand the relative contribution of each process to the planetary scale selection and slow eastward phase speed, we show the contributions from individual terms in the right hand side of Eq. 3 (Fig. 5). It is found that the planetary scale selection in the model is primarily attributed to the atmospheric radiative heating effect (Fig. 5a). The slow eastward phase speed, on the other hand, is a result of competition of eastward phase speed contributed by horizontal MSE advection, vertical MSE advection and PBL specific humidity tendency and westward phase speed contributed by the surface latent heat flux and the atmospheric radiation heating.

Figure 6 shows the relative contribution of each term to zonal phase speed for the most unstable mode (i.e., wavenumber 1). While horizontal MSE advection, vertical MSE advection and PBL moisture tendency contribute to an eastward phase speed of 4 m s^{-1}, 3 m s^{-1} and 1 m s^{-1}, respectively, the surface latent heat flux and atmospheric radiative

Table 1 Standard values of key parameters in the theoretical model

Symbol	Description	Standard value
ε	Damping coefficient in free atmosphere	10^{-6} s^{-1}
E	Ekman pumping coefficient	10^{-5} s^{-1}
ΔP_1	Depth of free atmosphere	800 hPa
ΔP_2	Half depth of free atmosphere	400 hPa
ΔP_B	Depth of boundary layer	100 hPa
C_1	Gravity wave speed for the first baroclinic mode	50 ms^{-1}
C_2	Gravity wave speed for the second baroclinic mode	26.2 ms^{-1}
x_1	Distance between stratiform and convective cloud center	1200 km
L_0	Meridional e-folding scale of $\langle m' \rangle$	1.1×10^3 km
$\bar{q}_s - \bar{q}_a$	Mean sea-air specific humidity difference	3.26 gkg^{-1}
b_1	Convective heating coefficient (Eq. 4)	4.43×10^{-10} m^2 kg^{-1} s^{-1}
b_2	Stratiform heating coefficient (Eq. 8)	3.96×10^{-11} m^2 kg^{-1} s^{-1}
α_1	Longwave radiative heating coefficient due to convective clouds	1×10^{-6} m^2 kg^{-1}
α_2	Longwave radiative heating coefficient due to stratiform clouds	2.5×10^{-7} m^2 kg^{-1}

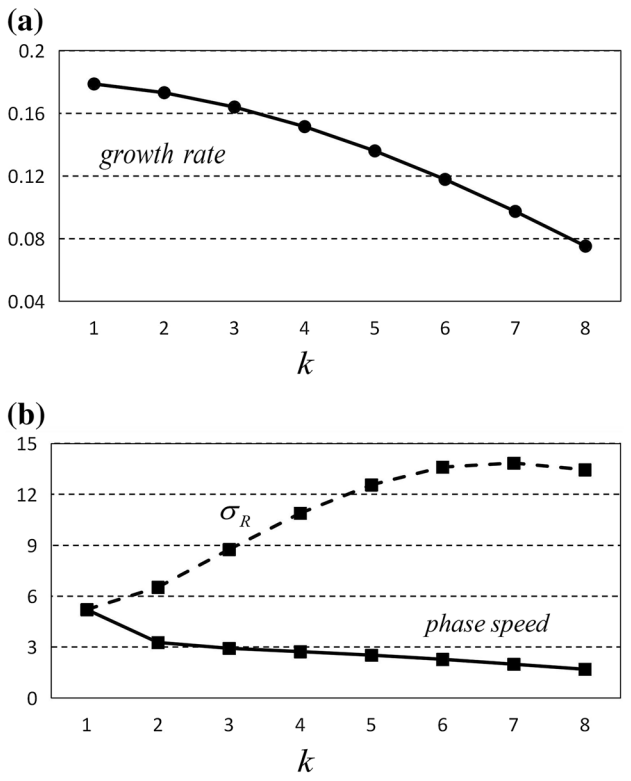

Fig. 4 **a** Growth rate (unit: day^{-1}) and **b** frequency σ_R (dashed line; unit: 1.57×10^{-7} s^{-1}) and phase speed (solid line; unit: m s^{-1}) as function of zonal wavenumber k

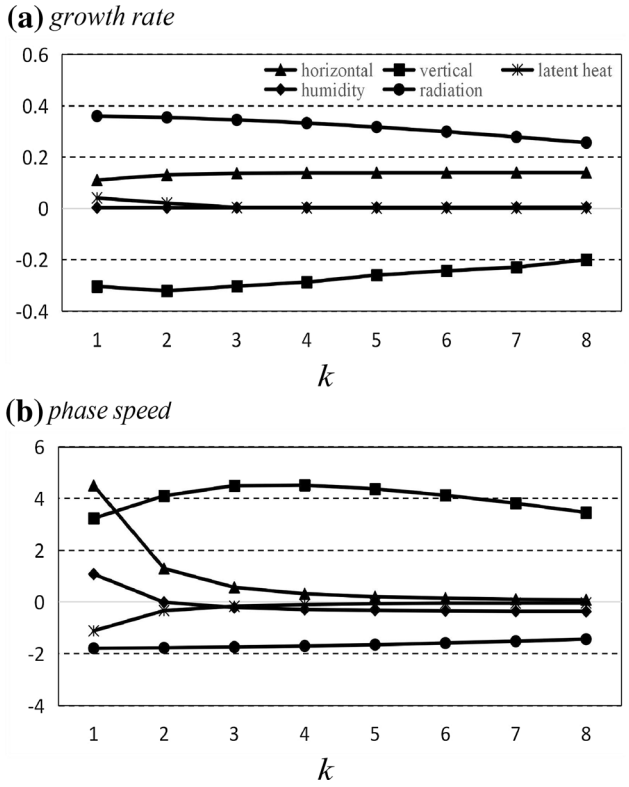

Fig. 5 **a** Growth rate (unit: day^{-1}) and **b** phase speed (unit: m s^{-1}) as function of zonal wavenumber k in the presence of horizontal MSE advection (triangular), vertical MSE advection (square), surface latent heat flux (stellate), PBL specific humidity tendency (diamond), and atmospheric radiative heating (circle)

heating contribute to a westward phase speed of 1 m s^{-1} and 2 m s^{-1}. As a result, the net effect is about 5 m s^{-1}. The relative contribution of horizontal and vertical advection, surface latent heat flux and atmospheric radiative heating to the eastward propagation in the simple theoretical model is quite consistent with the observational and general circulation model results (see Fig. 3 of Wang et al. 2017).

3.2 Structure of the most unstable mode

The horizontal structure of the most unstable mode is shown in left panel of Fig. 7, while the observed counterpart derived from ERA-I is shown in the right panel of Fig. 7. For MJO convective center located over 85°E, 0°N, meridional wind at 700 hPa shows pronounced equatorward flow to the west of MJO convective center and pronounced poleward flow to its east. The former is the part of Rossby wave response to the MJO deep convective heating, while the latter is the part of Rossby wave response to suppressed convective heating anomaly to the east of MJO convective center. Such a pattern in the simple theoretical model is quite similar to that derived from the observation.

The vertical velocity field at 300 hPa primarily reflects the zonal asymmetry between the ascending anomalies within

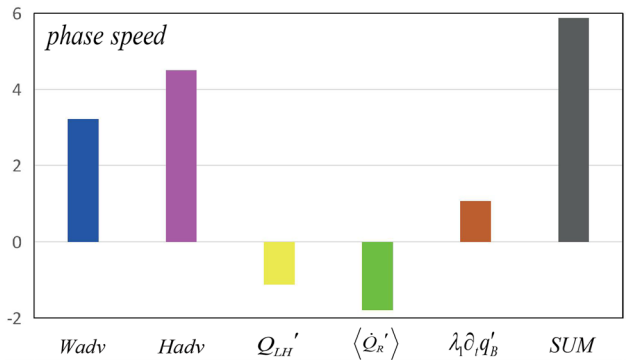

Fig. 6 Zonal phase speed (unit: m s^{-1}) caused by vertical MSE advection (Wadv), horizontal MSE advection (Hadv), surface latent heat fluxes (Q_{LH}'), atmospheric radiative heating ($\langle \dot{Q}_R' \rangle$), PBL specific humidity tendency ($\lambda_1 \partial_t q_B'$) and sum of the five terms (SUM)

the stratiform cloud in the rear and pronounced cloud-free descending anomalies in the front (see Fig. 6 of Wang et al. 2017). The simple model is able to capture the zonal asymmetric vertical velocity distribution.

The anomalous ascending motion at the top of PBL to the east of MJO convection reflects the phase leading

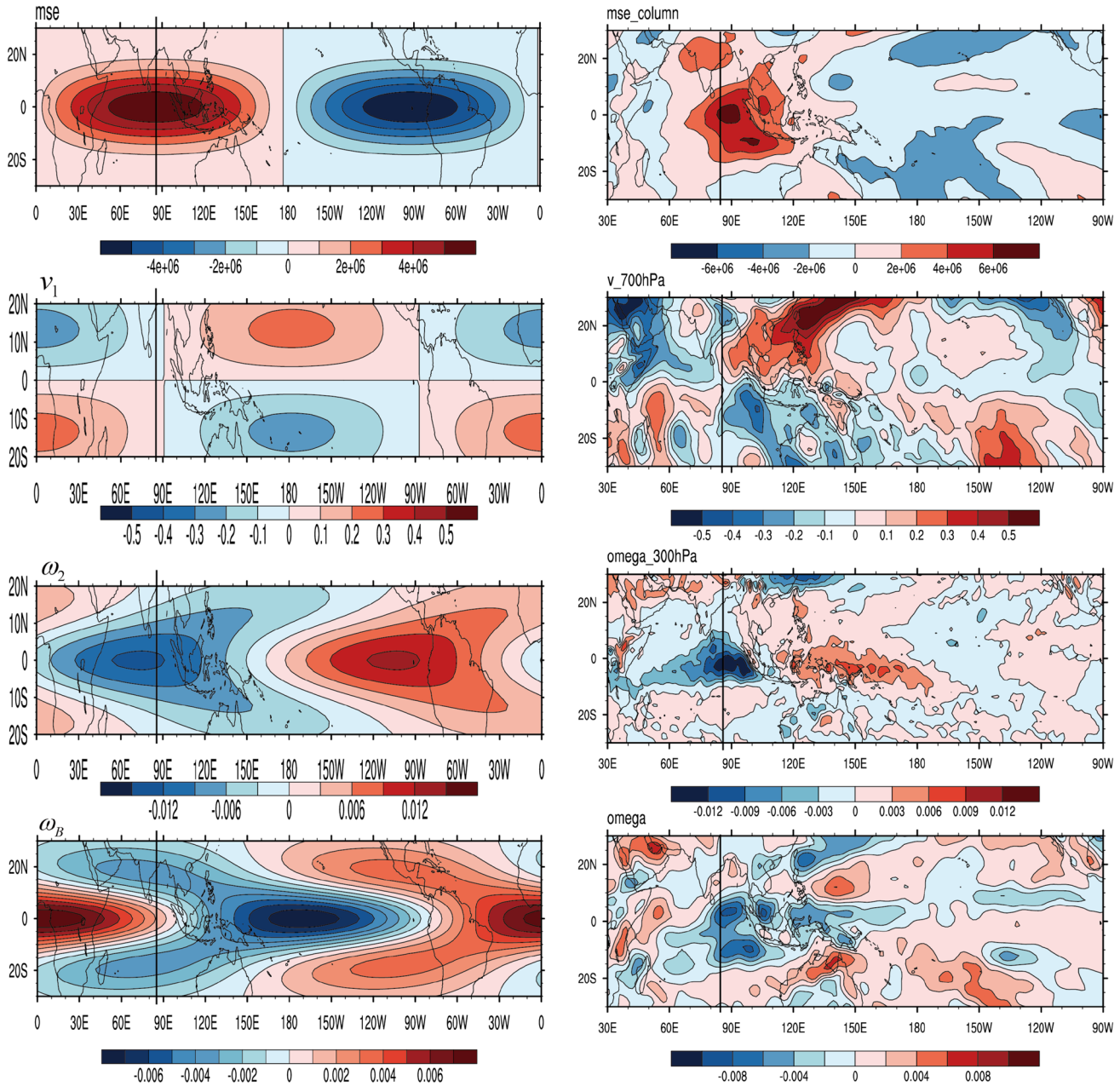

Fig. 7 Horizontal structure of the most unstable mode in the model (left) and observed counterpart (right). From top to bottom: column-integrated MSE (unit: J m^{-2}), meridional wind at 700 hPa (unit: m s^{-1}), vertical velocity at 300 hPa (unit: Pa s^{-1}), and vertical velocity (unit: Pa s^{-1}) at the top of PBL. The black line denotes the longitudinal position of MJO deep convection

of boundary layer convergence, which is caused by heating induced free-atmospheric Kelvin wave responses (Hsu and Li 2012). This boundary layer convergence process is critical in determining the PBL moistening (via the vertical advection of mean moisture) to the east of MJO convection. Such a phase-leading characteristic of PBL vertical velocity predicted by the simple theoretical model is seen in the observations.

To sum up, the most unstable mode has a circulation structure similar to the observed. Thus the simple model is able to reproduce the observed first and second baroclinic mode circulation and boundary layer wind fields reasonably well. However, it is worth mentioning that the meridional structure of the unstable mode was not predicted, rather specified from the observation. As a result, the unstable mode here is only referred to the zonal longwave selection.

3.3 Sensitivity of the model solution to key parameters

Several key parameters appear in the simple theoretical model. Among them are the zonal distance (x_1) between the MJO deep convective center and the center of the stratiform cloud in the rear and heating coefficients b_1 and b_2. As shown in Table 1, a standard value of 1200 km is used for x_1. To test how sensitive the model solution is to the parameter, an increase or a decrease of the value by 25% is tested, and the result is shown in Fig. 8. For all the three parameter values, the planetary scale selection remains the same, that is, the most unstable mode always appears at zonal wavenumber 1. With the decrease of x_1, the growth rate increases, while the phase speed decreases.

Similarly, the sensitivity test with an increase or a decrease of the heating coefficients b_1 and b_2 by 20% was done. Figure 9 shows the so-calculated growth rate and phase speed when both the heating coefficients are increased or decreased by 20%. Again the planetary scale selection is clearly presented in all the three cases. While the fundamental features of dependence of frequency and growth rate on wavenumber do not change much, both the growth rate and phase speed increase with the increase of the heating coefficients. In particular, the eastward phase speed is almost doubled when the heating coefficients increase by 20%, indicating that the eastward propagation is sensitive to the heating strength.

Another sensitivity test with or without the PBL humidity term in Eq. (3) was conducted. The result shows that without consideration of the PBL humidity tendency, eastward propagation speed decreases by 20.6% (i.e., from 5.2 m s^{-1} to 4.13 m s^{-1}) and maximum growth rate decreases by 1.7% (i.e., from 0.179 day^{-1} to 0.176 day^{-1}). This indicates that even from the moisture mode theory perspective, the asymmetric PBL moistening effect plays a role in eastward phase propagation, while it is of little importance in affecting overall MJO intensity.

4 Mechanisms for slow eastward propagation and planetary scale selection

In this section we briefly discuss mechanisms responsible for the slow eastward phase speed and planetary scale selection in the model. In particular, we will discuss specific physical processes through which horizontal MSE advection, vertical MSE advection and boundary layer moistening promote an eastward phase speed, while

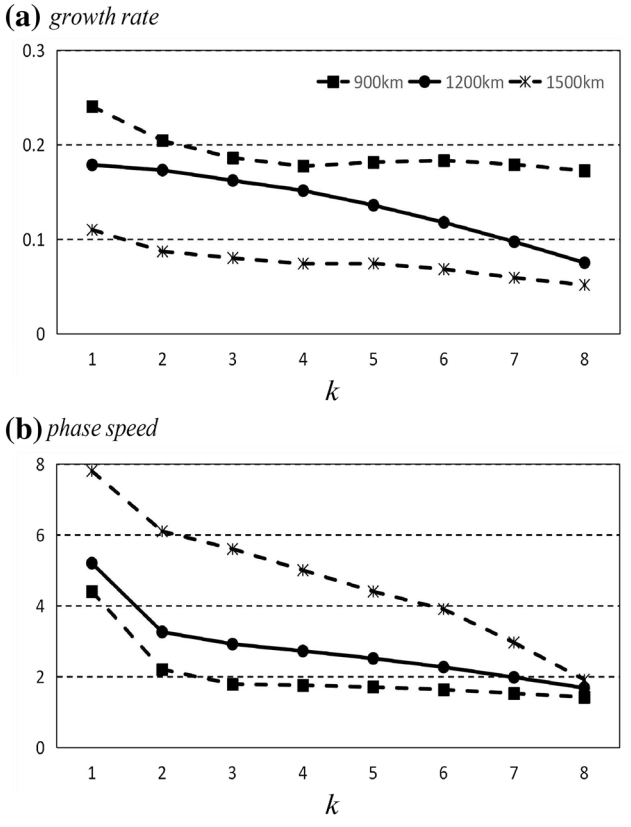

Fig. 8 **a** Growth rate (unit: day^{-1}) and **b** phase speed (unit: m s^{-1}) as function of zonal wavenumber k when different values (900 km, 1200 km and 1500 km) of x_1 are used

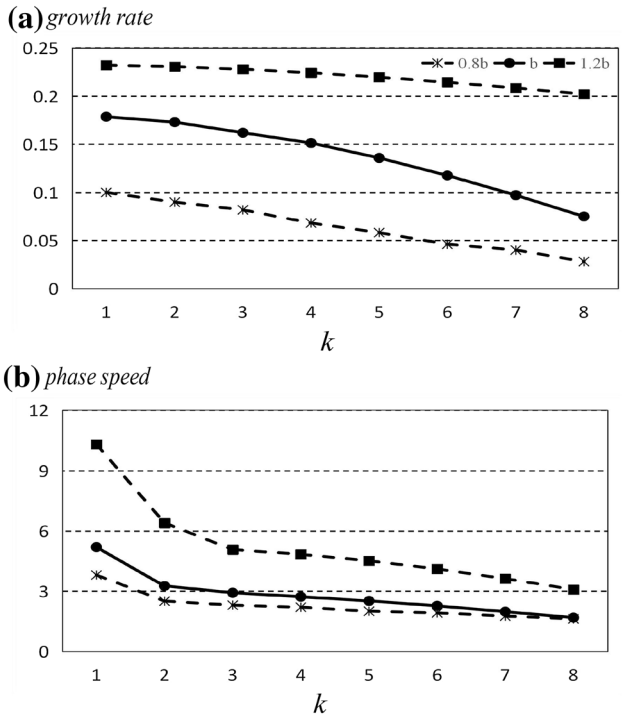

Fig. 9 As in Fig. 8, except that different values of the heating coefficients b (b_1 and b_2) are used

surface latent heat flux and atmospheric radiative heating contribute to a westward phase speed.

4.1 Mechanism for slow eastward propagation

It is seen clearly from Fig. 6 that horizontal MSE advection, vertical MSE advection and boundary layer moistening process promote eastward propagation. What are physical mechanisms behind the analytical results? In the following we will examine the role of each process from the spatial phase difference point of view.

Figure 10 shows the spatial phase difference between column-integrated MSE anomaly and MSE tendency caused by horizontal MSE advection. As the MJO convective center is located near phase 90, maximum MSE tendency due to meridional advection appears at phase 180. It is the near quadrature phase relation that causes the system moving eastward.

The cause of a positive MSE tendency to the east of the MJO convective center is attributed to poleward meridional wind anomalies (Fig. 7) that advect high mean MSE away from the equator. The anomalous poleward flow results from Gill type response to a suppressed convective anomaly in the front, which is a result of Kelvin wave induced subsidence. A negative MSE tendency center to the west of the MJO convection is a result of mean MSE advection by anomalous equatorward wind as part of Rossby wave response to MJO deep convection.

The phase relationship between the column-integrated MSE and the vertical advection induced MSE tendency fields is shown in Fig. 11b. The center of the MSE tendency due to the vertical advection appears east of phase 270. As a result, a positive tendency appears at phase 180. This promotes eastward propagation for the MJO mode. In the presence of stratiform cloud behind the MJO deep convection, there is anomalous upward motion to the west in the upper level and downward motion in the lower level (Wang et al. 2017). Given the mean MSE vertical profile, this anomalous vertical velocity distribution would lead to a negative vertical MSE advection west of the column integrated MSE center (Fig. 11a). To the east, the stratiform heating induced second baroclinic mode causes a descending anomaly in the upper level and an ascending anomaly in the lower level, which generates a local positive MSE tendency. As a result, the vertical MSE advection promotes eastward propagation.

The phase relationship between the column-integrated MSE and the part of the MSE tendency caused by PBL moistening is shown in Fig. 12. Again a positive tendency appears at phase 180, indicating an eastward phase speed. The positive tendency is attributed to the occurrence of PBL convergence due to heating induced free-atmospheric wave effect (Hsu and Li 2012).

It is seen from the previous section that the surface latent heat flux and atmospheric radiative heating promote a westward phase speed, which slows down the overall eastward propagation. Figure 13b shows the spatial phase relation between the column-integrated MSE and MSE tendency caused by the latent heat flux. A positive tendency appears near phase 0, indicating that this process indeed promotes

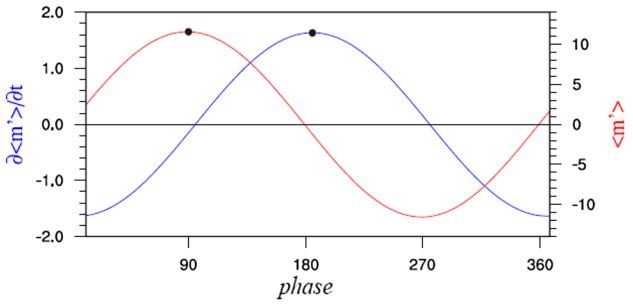

Fig. 10 Phase relationship between column-integrated MSE (unit: 10^6 kg s^{-2}; red line; right y-axis) and MSE tendency (unit: kg s^{-3}; blue line; left y-axis) caused by horizontal MSE advection for the most unstable mode. Horizontal ordinate is wave phase. The black dots represent the peaks of the MSE or MSE tendency curves

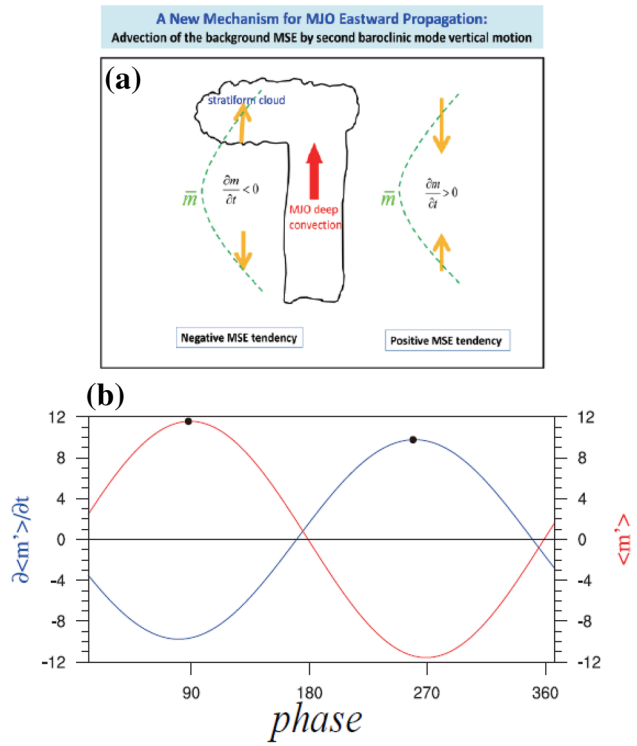

Fig. 11 **a** Schematic diagram illustrating the role of vertical MSE advection in contributing to zonal asymmetry of MSE tendency and MJO eastward propagation (from Fig. 10 of Wang et al. 2017). **b** Phase relation between column-integrated MSE (unit: 10^6 kg s^{-2}; red line; right y-axis) and MSE tendency (unit: kg s^{-3}; blue line; left y-axis) caused by vertical MSE advection in the model

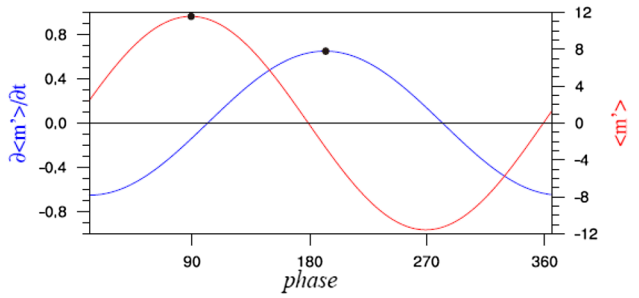

Fig. 12 As in Fig. 10 except for the MSE tendency caused by PBL moistening

westward propagation. The cause of this westward tendency is attributed to the distribution of anomalous zonal wind at low level. According to Gill (1980) response, anomalous westerly (easterly) appears to the west (east) of the MJO convective center (Fig. 13a). Given the mean westerly over the warm pool, the surface latent heat flux is increased (decreased) to the west (east) of the MJO convection, which promotes westward propagation.

The spatial phase relation between the column-integrated MSE and MSE tendency caused by atmospheric radiative heating for the most unstable mode (i.e., wavenumber 1) is illustrated at top panel of Fig. 14. Due to the presence of upper-level stratiform cloud in the rear, the positive MSE tendency is shifted slightly to the west. This promotes a westward phase speed.

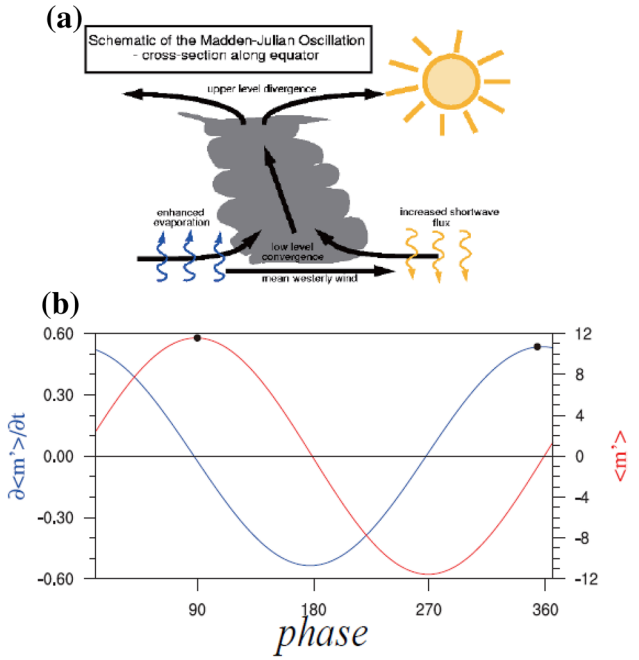

Fig. 13 **a** Schematic diagram illustrating surface wind and latent heat flux anomalies associated with the MJO. **b** As in Fig. 10 except for the MSE tendency caused by the surface latent heat flux effect in the model

4.2 Mechanism for planetary scale selection

As shown in Fig. 5a, the main contribution of planetary zonal scale selection of the MJO mode in the simple analytical model arises from the atmospheric radiation heating term. To illustrate how this mechanism works, the phase differences between the column-integrated MSE and radiation induced MSE tendency for zonal wavenumber 1, 4 and 7 are plotted in Fig. 14 for comparison. Note that the phase difference between the maximum MSE center and the maximum MSE tendency center increases with increased wavenumber. Meanwhile the amplitude of the MSE tendency decreases with increased wavenumber. Because of both the phase shift and the amplitude decrease, the value of the MSE tendency projected into the MSE center decreases with increased

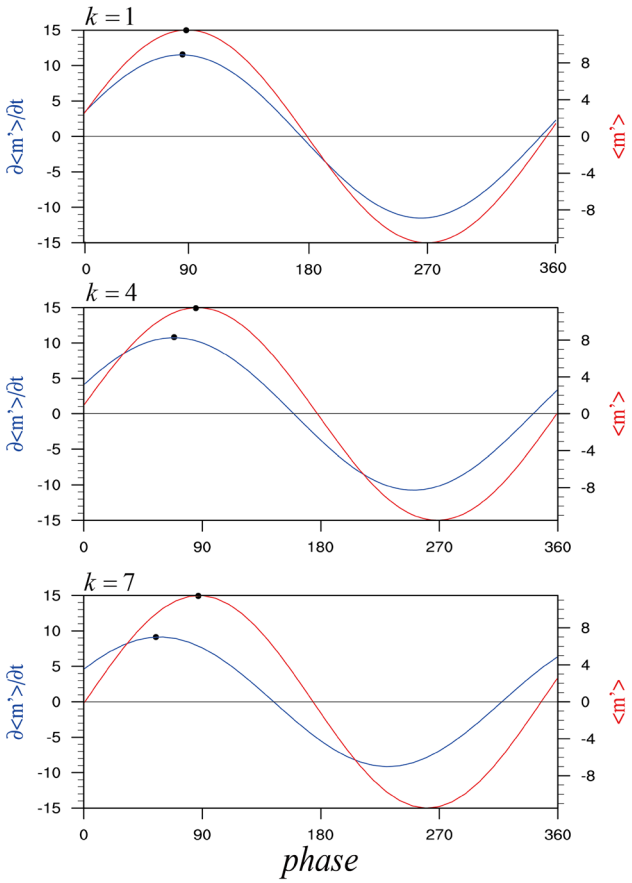

Fig. 14 Phase relationships between column-integrated MSE (unit: 10^6 kg s^{-2}; red line; right y-axis) and MSE tendency (unit: kg s^{-3}; blue line; left y-axis) caused by atmospheric radiative heating process. From top to bottom: model solutions for wavenumber-1, 4 and 7, respectively. Horizontal ordinate is wave phase. The black dots represent the peaks of the MSE or MSE tendency curves

wavenumber. As a result, the growth rate of the MJO mode decreases with increased zonal wavenumber.

As the phase shift is primarily attributed to the stratiform heating in the rear of the MJO convection, we point out the important role the stratiform cloud plays in scale selection. For given a fixed length between the center of the stratiform cloud and the MJO deep convective center, a greater wave length implies a smaller phase difference. Given that longwave radiative effect of clouds tends to warm the air column and thus increases the MSE, a smaller phase difference implies a greater tendency of the MSE and thus a greater growth rate of the MJO mode.

In addition to the column integrated radiative heating, the surface latent heat flux also plays a minor role in favoring longwave selection. The horizontal and vertical MSE advection terms, on the other hand, favor the growth of smaller scale waves (Fig. 5). But the final outcome is that the atmospheric radiative effect dominates. It follows that while MJO planetary scale selection and amplitude growth are primarily controlled by the atmospheric radiative process, its phase propagation is more controlled by horizontal and vertical MSE advection.

5 Conclusion and discussion

A theoretical model that involves the coupling of the moisture mode thermodynamics with equatorial dynamics of free-atmospheric first and second baroclinic modes and planetary boundary layer was constructed to understand the fundamental cause of the MJO propagation and scale selection. An essential part of the simple model is column integrated MSE tendency, which is determined by horizontal and vertical MSE advection, radiation heating, surface latent heat flux, and boundary layer moistening. The dynamic fields are determined based on the first principal. Under a realistic parameter regime, the simple theoretical model reproduces a most unstable mode with zonal wavenumber 1 structure and a slow eastward phase speed of about 5 m s^{-1}. The horizontal circulation pattern of the most unstable mode resembles well the observed MJO structure. For instance, there is low-level equatorward (poleward) flow to the west (east) of MJO convective center, and PBL convergence and upward motion lead the MJO convection.

The slow eastward propagation in the simple model is the competition result of eastward propagation induced by horizontal MSE advection, vertical MSE advection and PBL moistening and westward propagation induced by atmospheric radiative heating and surface latent heat flux. While the horizontal advection is primarily attributed to advection of mean MSE by anomalous first baroclinic mode meridional wind (Kim et al. 2014), the vertical advection is attributed to advection of mean MSE by anomalous second baroclinic mode vertical velocity (Wang et al. 2017).

Physical mechanisms that contribute to the eastward propagation are summarized as follows. In response to MJO deep convective heating, low-level cyclonic gyres with equatorward flow appear to the west of MJO convection, as a Rossby wave response. To the east, a Kelvin wave response leads to anomalous subsidence and negative heating anomalies, which induce low-level poleward flow. As the maximum mean MSE appears near the equator, the anomalous meridional flow would lead to a positive MSE advection to the east and a negative tendency to the west, which favors for eastward propagation. Meanwhile, the presence of upper-level stratiform clouds in the rear of MJO convection causes zonally asymmetric second baroclinic mode vertical velocity response, with anomalous descending motion in the upper level and ascending motion in the lower troposphere to the east and an opposite pattern to the west. As the mean MSE has a minimum in middle troposphere, the second baroclinic mode vertical motion anomalies cause a positive MSE tendency to the east but a negative tendency to the west, promoting eastward propagation. The boundary layer moistening due to PBL convergence in front of MJO convection (Hsu and Li 2012) also favors an eastward phase speed. Surface latent heat flux and atmospheric radiation heating promote westward propagation, because both wind-induced latent heat flux and longwave radiative feedback due to upper-level stratiform clouds increase to the west of the MJO deep convection.

The planetary scale selection in the model is primarily determined by the atmospheric longwave radiative heating. In the presence of upper-level stratiform cloud in the rear, the model generates the strongest longwave radiative feedback when the MJO has a zonal wavenumber 1 structure. In contrast, horizontal and vertical MSE advection and boundary layer moistening processes favor the growth at shorter wave length. But these processes are overwhelmed by the atmospheric radiative process. As a result, the moisture-dynamics coupled mode favors planetary scale selection.

It is worth mentioning that a number of assumptions have been made in the simple analytical model, including a longitudinal phase difference between the MJO deep convective center and stratiform cloud in the rear and a simple meridional mode structure for the MSE. Strictly speaking, it is still a semi-empirical framework. A further effort to relax these assumptions by developing a conceptual model to mimic the stratiform cloud formation process and by resolving the model meridional structure explicitly is needed, in an attempt to improve the current theoretical model framework.

Acknowledgements This study is jointly supported by China National 973 project Grant 2015CB453200, NSF Grant AGS-16-43297, NOAA Grant NA18OAR4310298, and NSFC Grants 41875069/41575043.

This is SOEST contribution, IPRC contribution number 1388 and ESMC number 263.

Appendix

The free-atmosphere first-baroclinic-mode governing equations may be written as:

$$\begin{cases} \varepsilon u_1' - \beta y v_1' = -\partial_x \phi_1' \\ \beta y u_1' = -\partial_y \phi_1' \\ \varepsilon \phi_1' + C_1^2\left(\partial_x u_1' + \partial_y v_1'\right) = -\frac{\dot{Q}_1'}{C_p}\frac{R\Delta P_1}{2P_1} \end{cases} \tag{18}$$

Because observed MJO circulation exhibits a large-scale characteristic in both the zonal and meridional directions, we keep the lowest three meridional modes (Hermite functions) for anomalous wind and geopotential height fields. Therefore, one may derive the following solutions for Eq. (18):

$$\begin{cases} u_1' = \left[U_{10}H_0(y) + U_{12}H_2(y)\right]e^{-\frac{y^2}{2}\frac{\beta}{C_1}}e^{i(kx-\sigma t)} \\ v_1' = V_{11}H_1(y)e^{-\frac{y^2}{2}\frac{\beta}{C_1}}e^{i(kx-\sigma t)} \\ \phi_1' = \left[\phi_{10}H_0(y) + \phi_{12}H_2(y)\right]e^{-\frac{y^2}{2}\frac{\beta}{C_1}}e^{i(kx-\sigma t)} \\ \frac{\dot{Q}_1'}{C_p}\frac{R\Delta P_1}{2P_1} = b_1 M H_0(y)e^{-\frac{y^2}{2}\frac{\beta}{C_1}}e^{i(kx-\sigma t)} \end{cases} \tag{19}$$

where k is zonal wavenumber, σ is a complex parameter with its real part representing frequency and its imagine part representing growth rate, y denotes meridional distance away from the equator, and M represents the amplitude of the MSE anomaly at the equator. Subscript 1 denotes the first baroclinic mode variable.

Hermite function $H_m(y)$ satisfies the following meridional profiles:

$$\begin{cases} H_0(y) = 1 \\ H_1(y) = 2y\sqrt{\frac{\beta}{C_1}} \\ H_2(y) = 4y^2\frac{\beta}{C_1 - 2} \end{cases}.$$

Through a series of derivation, the meridional wind anomaly of the first baroclinic mode may be written as:

$$v_1' = -b_1 y M e^{-\frac{y^2}{2}\frac{\beta}{C_1}}e^{i(kx-\sigma t)}D_1 \tag{20}$$

where

$$D_1 = \frac{1}{\left[C_1^2\left(9\varepsilon^6 + 11C_1^4\varepsilon^2k^4 + 19C_1^2\varepsilon^4k^2 + C_1^6k^6\right)\right]} \cdot \left[\left(3\varepsilon^6 + 2C_1^4\varepsilon^2k^4 + 5C_1^2\varepsilon^4k^2 - C_1^5k^6 - C_1^3\varepsilon^2k^4\right) + i\left(4C_1\varepsilon^5k + 5C_1^3\varepsilon^3k^3 + 3C_1^2\varepsilon^3k^3 + 3C_1^4\varepsilon k^5 + C_1^5\varepsilon k^5\right)\right]$$

The second-baroclinic-mode governing equations may be written as:

$$\begin{cases} \varepsilon u_2' - \beta y v_2' = -\partial_x \phi_2' \\ \beta y u_2' = -\partial_y \phi_2' \\ \varepsilon \phi_2' + C_2^2\left(\partial_x u_2' + \partial_y v_2'\right) = -\frac{\dot{Q}_2'}{C_p}\frac{R\Delta P_2}{2P_2} \end{cases} \tag{21}$$

Using the same meridional truncation approach, one may derive the solutions for the second baroclinic mode motion:

$$\begin{cases} u_2' = \left[U_{20}H_0(y) + U_{22}H_2(y)\right]e^{-\frac{y^2}{2}\frac{\beta}{C_2}}e^{i(kx-\sigma t)} \\ v_2' = V_{22}H_2(y)e^{-\frac{y^2}{2}\frac{\beta}{C_2}}e^{i(kx-\sigma t)} \\ \phi_2' = \left[\phi_{20}H_0(y) + \phi_{22}H_2(y)\right]e^{-\frac{y^2}{2}\frac{\beta}{C_2}}e^{i(kx-\sigma t)} \\ \frac{\dot{Q}_2'}{C_p}\frac{R\Delta P_2}{2P_2} = b_2 M H_0(y)e^{-\frac{y^2}{2}\frac{\beta}{C_2}}e^{i\left[k(x+x_1)-\sigma t\right]} \end{cases} \tag{22}$$

where x_1 represents the longitudinal distance between the MJO deep convective center and the stratiform cloud center in the rear. The sensitivity of the model solution to this parameter was tested.

Through a series of derivation, the vertical velocity anomaly of the second baroclinic mode may be written as:

$$\omega_2' = -\Delta P_2 b_2 M e^{-\frac{y^2}{2}\frac{\beta}{C_2}}e^{i(kx-\sigma t)}e^{i(kx_1)}D_2(y^2) \tag{23}$$

where

$$D_2(y^2) = \frac{1}{2C_2^2\left(9\varepsilon^6 + 11C_2^4\varepsilon^2k^4 + 19C_2^2\varepsilon^4k^2 + C_2^6k^6\right)} \left\{\left[\left(3\varepsilon^6 + 11C_2^2\varepsilon^4k^2 + 9C_2^4\varepsilon^2k^4 + C_2^6k^6\right) + i\left(4C_2\varepsilon^5k + 4C_2^3\varepsilon^3k^3\right)\right] - y^2\left[\left(3\varepsilon^6\frac{\beta}{C_2} + 6\varepsilon^4C_2k^2\beta + 3\varepsilon^2C_2^3k^4\beta + i\left(\varepsilon^5k\beta + 2\varepsilon^3C_2^3k^3\beta + \varepsilon C_2^4k^5\beta\right)\right)\right]\right\}$$

To calculate the surface latent heat flux and PBL moisture tendency contribution, a vertically integrated PBL model is introduced:

$$\begin{cases} Eu_B' - \beta y v_B' = -\partial_x \phi_B' \\ Ev_B' + \beta y u_B' = -\partial_y \phi_B' \\ \partial_x u_B' + \partial_y v_B' + \frac{\omega_B'}{\Delta P_B} = 0 \\ \phi_B' = \phi_1' - \phi_2' \end{cases}, \tag{24}$$

Through a series of derivation, anomalous zonal wind at PBL, u'_B, and anomalous vertical velocity at top of PBL, ω'_B, may be written as:

$$u'_B = b_1 M e^{-\frac{y^2}{2}\frac{\beta}{C_1}} e^{i(kx-\sigma t)} D_3(y^2) - b_2 M e^{-\frac{y^2}{2}\frac{\beta}{C_2}} e^{i(kx-\sigma t)} e^{ikx_1} D_4(y^2) \tag{25}$$

$$\begin{aligned}\omega'_B = {} & \Delta P_B b_1 M e^{-\frac{y^2}{2}\frac{\beta}{C_1}} e^{i(kx-\sigma t)} D_5(y^2) \\ & + \Delta P_B b_2 M e^{-\frac{y^2}{2}\frac{\beta}{C_2}} e^{i(kx-\sigma t)} e^{ikx_1} D_6(y^2)\end{aligned} \tag{26}$$

where

$$\begin{aligned}D_3(y^2) = {} & \frac{1}{\left(E^2+y^2\right)\left(9\varepsilon^6+11C_1^4\varepsilon^2k^4+19C_1^2\varepsilon^4k^2+C_1^6k^6\right)} \\ & \left\{E\left[4C_1\varepsilon^4k^2+4C_1^3\varepsilon^2k^4+i\left(6\varepsilon^5k+8C_1^2\varepsilon^3k^3+2C_1^4\varepsilon k^5\right)\right]\right. \\ & +y^2\frac{\beta}{C_1}E\left[-\left(C_1\varepsilon^4k^2+2C_1^3\varepsilon^2k^4+C_1^5k^5\right)\right. \\ & \left.+i\left(3\varepsilon^5k+6C_1^2\varepsilon^3k^3+3C_1^4\varepsilon k^5\right)\right] \\ & +\beta^2y^2\left[\left(6C_1\varepsilon^3k^2+4C_1^3\varepsilon k^4-2C_1\varepsilon^3k^3\right)\right. \\ & \left.\left.+i\left(6\varepsilon^4k+8C_1^2\varepsilon^2k^3+2C_1^4k^5\right)\right]\right\}\end{aligned}$$

$$\begin{aligned}D_4(y^2) = {} & \frac{1}{\left(E^2+y^2\right)\left(9\varepsilon^6+11C_2^4\varepsilon^2k^4+19C_2^2\varepsilon^4k^2+C_2^6k^6\right)} \\ & \left\{E\left[4C_2\varepsilon^4k^2+4C_2^3\varepsilon^2k^4+i\left(6\varepsilon^5k+8C_2^2\varepsilon^3k^3+2C_2^4\varepsilon k^5\right)\right]\right. \\ & +y^2\frac{\beta}{C_2}E\left[-\left(C_2\varepsilon^4k^2+2C_2^3\varepsilon^2k^4+C_2^5k^5\right)\right. \\ & \left.+i\left(3\varepsilon^5k+6C_2^2\varepsilon^3k^3+3C_2^4\varepsilon k^5\right)\right] \\ & +\beta^2y^2\left[\left(6C_2\varepsilon^3k^2+4C_2^3\varepsilon k^4-2C_2\varepsilon^3k^3\right)\right. \\ & \left.\left.+i\left(6\varepsilon^4k+8C_2^2\varepsilon^2k^3+2C_2^4k^5\right)\right]\right\}\end{aligned}$$

$$\begin{aligned}D_5(y^2) = {} & \frac{1}{\left(E^2+\beta^2y^2\right)\left(9\varepsilon^6+11C_1^4\varepsilon^2k^4+19C_1^2\varepsilon^4k^2+C_1^6k^6\right)} \\ & \left\{E\left[-\left(6\varepsilon^5k^2+8C_1^2\varepsilon^3k^4+2C_1^4\varepsilon k^6\right)\right.\right. \\ & \left.+i\left(6C_1\varepsilon^4k^3+4C_1^3\varepsilon^2k^5-2C_1\varepsilon^4k^3\right)\right] \\ & +2\beta(E-\varepsilon)\left[\left(3C_1\varepsilon^3k^2+2C_1^3\varepsilon k^4-C_1\varepsilon^3k^3\right)\right. \\ & \left.+i\left(3\varepsilon^4k+4C_1^2\varepsilon^2k^3+C_1^4k^5\right)\right] \\ & -y^2\frac{\beta}{C_1}2\beta(E-\varepsilon)\left[\left(3C_1\varepsilon^3k^2+2C_1^3\varepsilon k^4-C_1\varepsilon^3k^3\right)\right. \\ & \left.+i\left(3\varepsilon^4k+4C_1^2\varepsilon^2k^3+C_1^4k^5\right)\right] \\ & -y^2\frac{\beta}{C_1}E\left[\left(6C_1^2\varepsilon^3k^4+3C_1^4\varepsilon k^6+3\varepsilon^5k^2\right)\right. \\ & \left.+i\left(C_1\varepsilon^4k^3+2C_1^3\varepsilon^2k^5+C_1^5k^7\right)\right] \\ & -y^2\beta^2\left[\left(8C_1^2\varepsilon^2k^4+2C_1^4k^6+6\varepsilon^4k^2\right)\right. \\ & \left.\left.-i\left(4C_1\varepsilon^3k^3+4C_1^3\varepsilon k^5\right)\right]\right\}\end{aligned}$$

$$\begin{aligned}D_6(y^2) = {} & \frac{1}{\left(E^2+\beta^2y^2\right)\left(9\varepsilon^6+11C_2^4\varepsilon^2k^4+19C_2^2\varepsilon^4k^2+C_2^6k^6\right)} \\ & \left\{E\left[-\left(6\varepsilon^5k^2+8C_2^2\varepsilon^3k^4+2C_2^4\varepsilon k^6\right)\right.\right. \\ & \left.+i\left(6C_2\varepsilon^4k^3+4C_2^3\varepsilon^2k^5-2C_2\varepsilon^4k^3\right)\right] \\ & +2\beta(E-\varepsilon)\left[\left(3C_2\varepsilon^3k^2+2C_2^3\varepsilon k^4-C_2\varepsilon^3k^3\right)\right. \\ & \left.+i\left(3\varepsilon^4k+4C_2^2\varepsilon^2k^3+C_2^4k^5\right)\right] \\ & -y^2\frac{\beta}{C_2}2\beta(E-\varepsilon)\left[\left(3C_2\varepsilon^3k^2+2C_2^3\varepsilon k^4-C_2\varepsilon^3k^3\right)\right. \\ & \left.+i\left(3\varepsilon^4k+4C_2^2\varepsilon^2k^3+C_2^4k^5\right)\right] \\ & -y^2\frac{\beta}{C_2}E\left[\left(6C_2^2\varepsilon^3k^4+3C_2^4\varepsilon k^6+3\varepsilon^5k^2\right)\right. \\ & \left.+i\left(C_2\varepsilon^4k^3+2C_2^3\varepsilon^2k^5+C_2^5k^7\right)\right] \\ & -y^2\beta^2\left[\left(8C_2^2\varepsilon^2k^4+2C_2^4k^6+6\varepsilon^4k^2\right)\right. \\ & \left.\left.-i\left(4C_2\varepsilon^3k^3+4C_2^3\varepsilon k^5\right)\right]\right\}\end{aligned}$$

The column integrated MSE tendency equation may be written as:

$$\begin{aligned}\left\langle \partial_t m' \right\rangle = {} & \frac{\Delta P_2}{g}\left(-v'_1\partial_y\bar{m}\right)\Big|_{p=700\,\mathrm{hPa}} - \frac{\Delta P_1}{g}\left(\omega'_2\partial_p\bar{m}\right)\Big|_{p=300\,\mathrm{hPa}} \\ & + \alpha\left\langle m' \right\rangle + \rho_a C_E L_v\left(\bar{q}_s-\bar{q}_a\right)\frac{\bar{u}_B u'_B}{\left|\bar{V}_B\right|} - L_v\frac{\Delta P_B}{g}\omega'_B\partial_p\bar{q}_B\end{aligned} \tag{27}$$

Assuming a Gausian distribution for $\langle m' \rangle = M\, e^{-\frac{y^2}{2L_0^2}} e^{i(kx-\sigma t)}$, and integrating Eq. (27) meridionally from $-L_0$ to L_0, one may derive an analytical solution for frequency σ_R and growth rate σ_I respectively:

$$\begin{aligned}\sigma_R = {} & \frac{-\delta_2 b_1 C_0^2\left(B_1B_4+B_2B_3\right)}{\delta_1 C_1^3\left(B_1^2+B_2^2\right)} - \alpha_2\sin\left(kx_1\right) \\ & + \frac{-b_2C_0^2}{\delta_1 C_2^2\sqrt{\beta C_2}\left(B_1^2+B_2^2\right)} \\ & \times\left\{\cos\left(kx_1\right)\left[\delta_3\frac{\beta}{C_2}\left(B_2B_5-B_1B_6\right)+\delta_4\left(B_2B_7+B_1B_8\right)\right]\right. \\ & \left.+\sin\left(kx_1\right)\left[\delta_3\frac{\beta}{C_2}\left(B_2B_6+B_1B_5\right)-\delta_4\left(B_2B_8-B_1B_7\right)\right]\right\} \\ & + \frac{1}{\delta_1\left(B_9^2+B_{10}^2\right)}\left\{b_1\delta_5\left[2\beta^2C_1k^2B_{10}-B_9\left(E\frac{\beta}{C_1}\varepsilon^2k\right.\right.\right. \\ & \left.\left.\left.+E\beta C_1k^3+2\beta^2\varepsilon k\right)\right]+2E\varepsilon^2kb_1\delta_6\left(B_{10}-B_9\right)\right. \\ & -b_1\delta_7B_{10}\left[-2E\varepsilon^2k^2+2\beta(E-\varepsilon)C_1k^2\right]+b_1\delta_8B_{10} \\ & \times\left[2\beta(E-\varepsilon)C_1k^2+E\left(C_1^2k^4+\varepsilon^2k^2\right)+\beta C_1 2\varepsilon k^2\right] \\ & +b_1\delta_7B_9\left[2EC_1\varepsilon k^3+2\beta(E-\varepsilon)\varepsilon k\right]-b_1\delta_8B_9 \\ & \left.\times\left[2\beta(E-\varepsilon)\varepsilon k-2\beta C_1^2k^3\right]\right\}\end{aligned} \tag{28}$$

$$\sigma_I = \frac{\delta_2 b_1 C_0^2 \left(B_1 B_3 - B_2 B_4\right)}{\delta_1 C_1^3 \left(B_1^2 + B_2^2\right)} + \alpha_1 + \alpha_2 \cos\left(kx_1\right)$$
$$+ \frac{b_2 C_0^2}{\delta_1 C_2^2 \sqrt{\beta C_2}\left(B_1^2 + B_2^2\right)}$$
$$\times \left\{ \cos\left(kx_1\right)\left[\delta_3 \frac{\beta}{C_2}\left(B_1 B_5 + B_2 B_6\right) + \delta_4\left(B_1 B_7 - B_2 B_8\right)\right]\right.$$
$$\left. + \sin\left(kx_1\right)\left[\delta_3 \frac{\beta}{C_2}\left(B_1 B_6 - B_2 B_5\right) - \delta_4\left(B_1 B_8 + B_2 B_7\right)\right]\right\}$$
$$+ \frac{1}{\delta_1\left(B_9^2 + B_{10}^2\right)}\left\{b_1 \delta_5\left[2\beta^2 C_1 k^2 B_9 + B_{10}\right.\right.$$
$$\left.\left.\left(E\frac{\beta}{C_1}\varepsilon^2 k + E\beta C_1 k^3 + 2\beta^2 \varepsilon k\right)\right] + 2E\varepsilon^2 k b_1 \delta_6\left(B_9 + B_{10}\right)\right.$$
$$- b_1 \delta_7 B_9\left[-2E\varepsilon^2 k^2 + 2\beta(E-\varepsilon)C_1 k^2\right] + b_1 \delta_8 B_9$$
$$\times\left[2\beta(E-\varepsilon)C_1 k^2 + E\left(C_1^2 k^4 + \varepsilon^2 k^2\right) + \beta C_1 2\varepsilon k^2\right]$$
$$- b_1 \delta_7 B_{10}\left[2EC_1 \varepsilon k^3 + 2\beta(E-\varepsilon)\varepsilon k\right]$$
$$+ b_1 \delta_8 B_{10}\left[2\beta(E-\varepsilon)\varepsilon k - 2\beta C_1^2 k^3\right] \quad (29)$$

where:

$$B_1 = 1.8 \times 10^7 \varepsilon^2 k^4 + 4.4 \times 10^4 \varepsilon^4 k^2 - 3.6 \times 10^9 k^6 + 1.4 \times 10^1 \varepsilon^6$$
$$B_2 = 6.3 \times 10^8 \varepsilon k^5 + 4.0 \times 10^6 \varepsilon^3 k^3 + 3.7 \times 10^2 \varepsilon^5 k$$
$$B_3 = 1.7 \times 10^4 \varepsilon^4 k^2 + 1.5 \times 10^7 \varepsilon^2 k^4 + 4.8 \times \varepsilon^6 + 3.6 \times 10^9 k^6$$
$$B_4 = 3.1 \times 10^5 \varepsilon^3 k^3 + 2.0 \times 10^2 \varepsilon^5 k + 3.4 \times 10^8 \varepsilon k^5$$
$$B_5 = 1.5 \times 10^4 \varepsilon^4 k^2 + 8.2 \times 10^6 \varepsilon^2 k + 4.8 \times \varepsilon^6$$
$$B_6 = 2.5 \times 10^5 \varepsilon^3 k^3 + 1.4 \times 10^8 \varepsilon k^5 + 8.0 \times 10^1 \varepsilon^5 k$$
$$B_7 = 2.4 \times 10^4 \varepsilon^4 k^2 + 2.8 \times 10^7 \varepsilon^2 k^4 + 4.8 \times \varepsilon^6 - 3.6 \times 10^9 k^6$$
$$B_8 = 2.7 \times 10^6 \varepsilon^2 k^3 - 6.3 \times 10^8 \varepsilon k^5 + 4.6 \times 10^1 \varepsilon^5 k$$
$$B_9 = 3\varepsilon^3 + 7.5 \times 10^3 \varepsilon k^2$$
$$B_{10} = -1.3 \times 10^5 k^3 - 5.0 \times 10^1 \varepsilon^2 k$$

$$\delta_1 = \int_{-L_0}^{L_0} e^{-\frac{y^2}{2L_0^2}} dy$$
$$\delta_2 = \int_{-L_0}^{L_0} \partial_y \bar{m}\Big|_{700\,\mathrm{hPa}} \frac{\Delta P_1}{g} y e^{-\frac{y^2}{2}\left(\frac{\beta}{C_1}\right)} dy$$
$$\delta_3 = -\Delta P_2 \int_{-L_0}^{L_0} \frac{\bar{m}_{100\,\mathrm{hPa}} + \bar{m}_{1000\,\mathrm{hPa}} - 2\bar{m}_{500\,\mathrm{hPa}}}{2g} y^2 e^{-\frac{y^2}{2}\left(\frac{\beta}{C_2}\right)} dy$$
$$\delta_4 = \Delta P_2 \int_{-L_0}^{L_0} \frac{\bar{m}_{100\,\mathrm{hPa}} + \bar{m}_{1000\,\mathrm{hPa}} - 2\bar{m}_{500\,\mathrm{hPa}}}{2g} e^{-\frac{y^2}{2}\left(\frac{\beta}{C_2}\right)} dy$$
$$\delta_5 = \int_{-L_0}^{L_0} \rho_a C_E L_v \left(\bar{q}_s - \bar{q}_a\right) \frac{\bar{u}_B}{\left|\bar{V}_B\right|} e^{-\frac{y^2}{2}\frac{\beta}{C_i}} y^2 \frac{1}{\left(E^2 + \beta^2 y^2\right)} dy$$
$$\delta_6 = \int_{-L_0}^{L_0} \rho_a C_E L_v \left(\bar{q}_s - \bar{q}_a\right) \frac{\bar{u}_B}{\left|\bar{V}_B\right|} e^{-\frac{y^2}{2}\frac{\beta}{C_i}} \frac{1}{\left(E^2 + \beta^2 y^2\right)} dy$$
$$\delta_7 = \int_{-L_0}^{L_0} -L_v \frac{\Delta P_B}{g} \partial_p \bar{q}_B e^{-\frac{y^2}{2}\frac{\beta}{C_i}} y^2 \frac{1}{\left(E^2 + \beta^2 y^2\right)} dy$$
$$\delta_8 = \int_{-L_0}^{L_0} -L_v \frac{\Delta P_B}{g} \partial_p \bar{q}_B e^{-\frac{y^2}{2}\frac{\beta}{C_i}} \frac{1}{\left(E^2 + \beta^2 y^2\right)} dy.$$

References

Adames ÁF, Kim D (2016) The MJO as a dispersive, convectively coupled moisture wave: theory and observations. J Atmos Sci 73(3):151125141200002

Biello JA, Majda AJ, Moncrieff MW (2007) Meridional momentum flux and superrotation in the multiscale IPESD MJO model. J Atmos Sci 64(5):1636–1651

Chang CP, Lim H (1988) Kelvin Wave-CISK: a possible mechanism for the 30-50 day oscillations. J Atmos Sci 45(11):1709–1720

Chao WC, Chen B (1999) The role of surface friction in tropical intraseasonal oscillation. Mon Weather Rev 129(4):268–270

Dee DP, Uppala SM, Simmons AJ et al (2011) The ERA-interim reanalysis: configuration and performance of the data assimilation system. Q J R Meteorol Soc 137(656):553–597

Emanuel KA (1987) An air-sea interaction model of intraseasonal oscillations in the tropics. J Atmos Sci 44(16):2324–2340

Fu X, Wang B (2009) Critical roles of the stratiform rainfall in sustaining the Madden–Julian oscillation: GCM experiments. J Clim 22(14):3939–3959

Gill AE (1980) Some simple solutions for heat-induced tropical circulation. Q J R Meteorol Soc 106(449):447–462

Hendon HH, Salby ML (1994) The life cycle of the Madden-Julian Oscillation. J Atmos Sci 51(15):2225–2237

Hsu P, Li T (2012) Role of the boundary layer moisture asymmetry in causing the eastward propagation of the Madden-Julian Oscillation. J Clim 25(14):4914–4931

Jiang X, Waliser DE, Xavier PK et al (2015) Vertical structure and physical processes of the Madden-Julian oscillation: exploring key model physics in climate simulations. J Geophys Res Atmos 120(10):4718–4748

Jones C, Weare BC (1996) The role of low-level moisture convergence and ocean latent heat fluxes in the Madden and Julian Oscillation: an observational analysis using ISCCP data and ECMWF analyses. J Clim 9(12):3086–3104

Khouider B, Majda AJ (2006) A simple multicloud parameterization for convectively coupled tropical waves. Part I: linear analysis. J Atmos Sci 63(4):1308–1323

Khouider B, Majda AJ (2007) A simple multicloud parameterization for convectively coupled tropical waves. Part II: nonlinear simulations. J Atmos Sci 64(2):381–400

Kiladis GN, Wheeler MC, Haertel PT et al (2009) Convectively coupled equatorial waves. Rev Geophys 47(2):RG2003. https://doi.org/10.1029/2008rg000266

Kim D, Kug JS, Sobel AH (2014) Propagating versus nonpropagating Madden-Julian Oscillation events. J Clim 27(1):111–125

Knutson TR (1986) Global-scale intraseasonal oscillations of outgoing longwave radiation and 250 mb zonal wind during northern hemisphere summer. Mon Weather Rev 114(114):605

Kuo HL (1974) Further studies of the parameterization of the influence of cumulus convection on large-scale flow. J Atmos Sci 31:1232–1240

Lau KM, Chan PH (1986) Aspects of the 40–50 day oscillation during the northern summer as inferred from outgoing longwave radiation. Mon Weather Rev 114(7):1354–1367

Lau NC, Lau KM (2010) The structure and propagation of intraseasonal oscillations appearing in a GFDL general circulation model. J Atmos Sci 43(19):2023–2047

Li T (2014) Recent advance in understanding the dynamics of the Madden-Julian Oscillation. J Meteorol Res 28(1):1–33

Li T, Hsu P-C (2018) Fundamentals of tropical climate dynamics, Text Book. Springer, pp 1–229. https://doi.org/10.1007/978-3-319-59597-9

Li T, Wang B (1994) The influence of sea surface temperature on the tropical intraseasonal oscillation: a numerical study. Mon Weather Rev 122(122):2349
Li T, Zhou C (2009) Planetary scale selection of the Madden-Julian Oscillation. J Atmos Sci 66(8):2429–2443
Liu F, Wang B (2017) Effects of moisture feedback in a frictional coupled Kelvin–Rossby wave model and implication in the Madden–Julian oscillation dynamics. Clim Dyn 48(1–2):513–522
Madden RA, Julian PR (1971) Detection of a 40-50 day oscillation in the zonal wind in the tropical pacific. J Atmos Sci 28(5):702–708
Madden RA, Julian PR (1972) Description of global-scale circulation cells in the tropics with a 40–50 day period. J Atmos Sci 29(6):1109–1123
Majda AJ, Biello JA (2004) A multiscale model for tropical intraseasonal oscillations. Proc Natl Acad Sci USA 101(14):4736–4741
Majda AJ, Stechmann SN (2009) The skeleton of tropical intraseasonal oscillations. Proc Natl Acad Sci 106:8417–8422
Maloney ED (2009) The moist static energy budget of a composite tropical intraseasonal oscillation in a climate model. J Clim 22(22):711–729
Maloney ED, Hartmann DL (1998) Frictional moisture convergence in a composite life cycle of the Madden–Julian oscillation. J Clim 11(9):2387–2403
Mapes BE (2000) Convective inhibition, subgrid-scale triggering energy and stratiform instability in a toy tropical wave model. J Atmos Sci 57:1515–1535
Moskowitz BM, Bretherton CS (2000) An analysis of frictional feedback on a moist equatorial Kelvin mode. J Atmos Sci 57(13):2188–2206
Neelin JD, Held IM (1987) Modeling tropical convergence based on the moist static energy budget. Mon Weather Rev 115(1):3–12
Rienecker MM et al (2011) MERRA: NASA's modern-era retrospective analysis for research and applications. J. Clim 24:3624–3648
Sobel A, Maloney E (2012) An idealized semi-empirical framework for modeling the Madden-Julian Oscillation. J Atmos Sci 69(5):1691–1705
Sobel A, Maloney E (2013) Moisture modes and the eastward propagation of the MJO. J Atmos Sci 70(1):187–192
Sperber KR (2003) Propagation and the vertical structure of the Madden Julian Oscillation. Mon Weather Rev 131(12):1200–1214
Thual S, Majda AJ, Stechmann SN (2015) Asymmetric intraseasonal events in the stochastic skeleton MJO model with seasonal cycle. Clim Dyn 45(3–4):603–618
Wang B (1988a) Comments on `An air-sea interaction model of intraseasonal oscillation in the tropics'. J Atmos Sci 45(22):3521–3525
Wang B (1988b) Dynamics of tropical low-frequency waves: an analysis of the moist Kelvin wave. J Atmos Sci 45(14):2051–2065
Wang B, Chen J-K (1989) On the zonal-scale selection and vertical structure of equatorial intraseasonal waves. Q J R Meteorol Soc 115:1301–1323
Wang B, Chen G (2017) A general theoretical framework for understanding essential dynamics of Madden–Julian oscillation. Clim Dyn 49(7–8):2309–2328
Wang B, Li T (1993) A simple tropical atmosphere model of relevance to short-term climate variations. J Atmos Sci 50(2):260–284
Wang B, Li T (1994) Convective interaction with boundary-layer dynamics in the development of a tropical intraseasonal system. J Atmos Sci 51(11):1386–1400
Wang L, Li T, Maloney E et al (2017) Fundamental causes of propagating and nonpropagating MJOs in MJOTF/GASS models. J Clim 30(10):3743–3769
Wang Lu, Li T, Nasuno T (2018) Impact of Rossby and Kelvin wave components on MJO eastward propagation. J Clim 31(17):6913–6931. https://doi.org/10.1175/JCLI-D-17-0749.1
Wei Y, Liu F, Mu M et al (2017) Planetary scale selection of the Madden–Julian oscillation in an air-sea coupled dynamic moisture model. Clim Dyn 50:1–16
Wheeler M, Kiladis GN (1999) Convectively coupled equatorial waves: analysis of clouds and temperature in the wavenumber-frequency domain. J Atmos Sci 56(3):374–399
Zhang C (2005) Madden-Julian oscillation. Rev Geophys 43(2):RG2003. https://doi.org/10.1029/2004RG000158
Zhang GJ, Song X (2009) Interaction of deep and shallow convection is key to Madden-Julian oscillation simulation. Geophys Res Lett 36(9):L09708